Mon. Not. R. Astron. Soc. **000**, 000–000 (0000) Printed 1 February 2008 (MN LATEX style file v1.4)

Supercluster Properties as a Cosmological Probe

V. Kolokotronis[1], S. Basilakos[2], M. Plionis[1].

[1] *Institute of Astronomy & Astrophysics, National Observatory of Athens, I. Metaxa & V. Pavlou, Palaia Penteli, 15236 Athens, Greece*

[2] *Astrophysics Group, Imperial College London, Blackett Laboratory, Prince Consort Road, London SW7 2BW, UK*

arXiv:astro-ph/0111044v1 2 Nov 2001

1 February 2008

ABSTRACT

We investigate the supercluster shape properties of the all-sky observed (Abell/ACO) and simulated (Virgo data) cluster catalogues using an approach based on differential geometry. We reliably identify rich superclusters by applying percolation statistics to both observed and mock cluster populations, the latter being constructed following the observational requirements of the Abell/ACO sample extended out to $z_{\rm max} \leq 0.114$. We apply a set of shape diagnostics in order to study in a thorough way the morphological features of superclusters with ≥ 8 cluster members. Results demonstrate that filamentarity is the dominant shape feature of superclusters. On comparing data and models, we show that the ΛCDM ($\Omega_\Lambda = 1 - \Omega_{\rm m} = 0.7$) model performs better than τCDM, which is excluded at a high confidence level, in agreement with other recent large scale structure studies.

Keywords: cosmology: theory - clusters - superclusters: general - large-scale structure of universe - Optical: clusters

1 INTRODUCTION

Superclusters of galaxies possess an eminent position in the structure hierarchy being the largest mass units we observe today. Since they have been seeded by density perturbations of the largest scale ($\sim 100\,h^{-1}$Mpc), they therefore constitute objects with which one can study the details of the fluctuations that gave rise to them (West 1989; Einasto et al. 1997). Additionally, we can obtain fruitful clues regarding the formation and evolution of the universe on the grandest scales and test cosmological models (Bahcall & Soneira 1984; Bahcall 1988; Frisch et al. 1995).

Numerous studies have been devoted not only to delineate the geometrical pattern of the universe as a whole (Zel'dovich, Einasto & Shandarin 1982; de Lapparent, Geller & Huchra 1991) confirming the picture of a well designed web-like network, but also to extract statistically complete supercluster catalogues in order to analyse their spatial distribution and morphological characteristics (Einasto et al. 2001a, b and references therein). However, only very recently (Sathyaprakash et al. 1998a; Basilakos, Plionis & Rowan-Robinson 2001 hereafter BPR) was any significance given to cosmological inferences from supercluster shape statistics. Sathyaprakash et al. (1998a) and BPR have used infrared galaxy samples (1.2 Jy and PSCz respectively), whereas we presently consider optical clusters (Abell + ACO).

A substantial number of geometrical and topological techniques have been applied to observational data to explore and assess clustering and superclustering at large ($> 100\,h^{-1}$Mpc) distances (Mecke et al. 1994; Sahni & Coles 1995; Yess & Shandarin 1996; Davé et al. 1997; Kerscher et al. 1997; BPR; Kerscher et al. 2001a, b and references therein). Nevertheless, an innovative method was devised recently (Sahni 1998; Sahni et al. 1998; Sathyaprakash et al. 1998b) and has been used with success, so far, in order to describe in detail the global geometrically complex features of large scale structure. The first time this new scheme was applied to astronomical data was in BPR, where it ascertained that the prominent feature of the large scale structures we see today is filamentarity, as it has also been observed in N-body simulations of gravitational clustering (Sathyaprakash et al. 1998b and references therein).

The aim of the present work is not to produce a reliable all-sky supercluster list. Such attempts have been copiously presented by other authors the last twenty five years or so, based either on optical or X–ray (ROSAT) cluster data (Bahcall & Soneira 1984; Batutski & Burns 1985; Postman, Huchra & Geller 1992; Cappi & Maurogordato 1992; Plionis, Valdarnini & Jing 1992; Zucca et al. 1993; Kalinkov & Kuneva 1995; Einasto et al. 2001a, b and references therein). The present analysis will focus on:

(i) whether or not superclusters verify the dominance of filamentarity as the basic trait of large scale structure and

(ii) if so, whether or not supercluster shape and size statistics can be used to test cosmological scenarios.

© 0000 RAS

The layout of the paper includes the following sections. We first present the observed and simulated datasets. In section 3, we discuss useful selection parameters of the observed sample, give a brief but sufficient report on the method used to investigate supercluster shape properties and comment on its stability. In section 4, we derive the morphological parameters of the real (Abell/ACO) and mock (Virgo) supercluster data and in section 5 we statistically compare data and dark matter (DM) models in an attempt to discriminate between possible structure formation scenarios. Finally, our concluding remarks are deserved in section 6.

2 THE DATASETS

2.1 The Abell/ACO cluster catalogue

In the present analysis we make use of the combined optical Abell/ACO cluster list (Abell 1958; Abell, Corwin & Olowin 1989), which contains 2712 and 1364 entries in the North and South hemispheres respectively but excludes the 1174 supplementary poor southern systems. We are utilising a redshift updated version of the catalogue up to a maximum redshift of $z_{\max} \leq 0.114$ and restrict ourselves to $|b| \geq 30^{\circ}$ to avoid severe selection biases (cf. sections 2 and 5 of Einasto et al. 2001b) and light absorption by the zone of avoidance (ZoA). After taking into account the double cluster entries, our final list includes 926 objects (523 Abell and 403 ACO), $\sim 80\%$ of which (733/926) have measured redshifts and are also in accordance with the above observational limits. Estimated redshifts are taken from Plionis & Valdarnini (1991).

All the above redshifts are heliocentric and transformed to the Local Group frame using the latest estimates for the Sun's galactic coordinates. Redshifts are converted to proper distances using a spatially flat background cosmology with $H_{\circ} = 100h\,\mathrm{km\,s^{-1}\,Mpc^{-1}}$ and $q_{\circ} = 0.5$. Thus, the redshift cutoff corresponds to a limiting distance $R_{\max} \leq 315h^{-1}\,\mathrm{Mpc}$.

2.2 The Hubble Volume simulations

For the purpose of our study it is necessary to use the largest up to date cosmological N-body simulations. This is the reason for our utilising the Virgo Consortium structure formation models (Frenk et al. 2000). Details of the simulations have been presented in Colberg et al. (2000) and Evrard et al. (2001 and references therein), so we only briefly discuss the main points here.

The Hubble Volume simulations follow the evolution of 10^9 particles in volumes comparable to the whole observable universe. We consider two spatially flat structure formation models, namely ΛCDM with $\Omega_{\Lambda} = 0.7$ and τCDM (massive τ-neutrino contribution). Further details of the two models are given in Table 1. The lengths of the boxes are $3h^{-1}$ Gpc and $2h^{-1}$ Gpc for the two cosmologies respectively. In both cases, the particle mass is $m_{\mathrm{p}} \geq 2.2 \times 10^{12}\,h^{-1}\,M_{\odot}$ and both models are normalised to the abundance of rich clusters at $z = 0$, i.e. $\sigma_8 = 0.55\,\Omega_{\mathrm{m}}^{-0.6}$ (Eke, Cole & Frenk 1996) and to COBE results.

Table 1. Parameters of the DM models.

Model	Ω_{m}	Ω_{Λ}	h	Γ	σ_8	L_{box}
τCDM	1.0	0.0	0.5	0.21	0.6	$2h^{-1}$Gpc
ΛCDM	0.3	0.7	0.7	0.17	0.9	$3h^{-1}$Gpc

Galaxy clusters are specified using a friend-of-friend algorithm with linking lengths of order 0.2 and 0.164 for τCDM and ΛCDM respectively. The sizes of simulation boxes certify that an appreciable number of independent "observers" will be identified within these vast volumes and the large number of simulated clusters ($> 10^6$) will ensure better statistics when supercluster shape properties are measured (see sections 4 and 5).

3 GEOMETRICAL AND SHAPE FORMALISM

3.1 Selection parameters

The supercluster catalogues for both observed and simulated data are constructed by using a constant size neighbourhood radius, i.e. a percolation radius (Zel'dovich et al. 1982), a scheme that has been successfully applied to similar kinds of studies. We place a sphere of a certain size around each cluster and then find all neighbouring spheres having an overlap region. In doing so, we join all clusters falling within the spheres which have common areas and do this for all clusters in the sample. In order to choose the optimal percolation radius, we have repeated the procedure by successively increasing the size of the sphere. At the end, we identify the radius that yields the maximum number of superclusters, which obviously occurs before the percolation of the superclusters themselves. The choice of this percolation radius (hereafter p_{r}) has been based on criteria similar to those of Einasto et al. (1994; 2001a, b and references therein).

To this end, we plot in Figure 1 the dependence of the number of superclusters on p_{r} for a variety of percolation radii for both data and models. Solid line corresponds to the Abell/ACO supercluster data, whereas dashed and dotted lines denote ΛCDM and τCDM respectively. Note, that this plot accounts for superclusters with at least 8 members, i.e. with multiplicity $k \geq 8$. As the p_{r} increases, the supercluster number increases accordingly reaching a maximum at radii between $25h^{-1}$ Mpc and $32h^{-1}$ Mpc. At larger radii, superclusters start connecting with each other and at even larger radii, we reach the point of superconnectivity with only a few (≤ 5) huge objects pervading the total volume available. We, therefore, choose to work with $p_{\mathrm{r}} = 27h^{-1}\,\mathrm{Mpc}$, which is a value well away from the superconnectivity limit ($\geq 33h^{-1}\,\mathrm{Mpc}$). Notice that our value is consistent with other recent analyses (Einasto et al. 1994; Einasto et al. 1997).

Another observational parameter we wish to compute is the number density of the Abell and ACO clus-

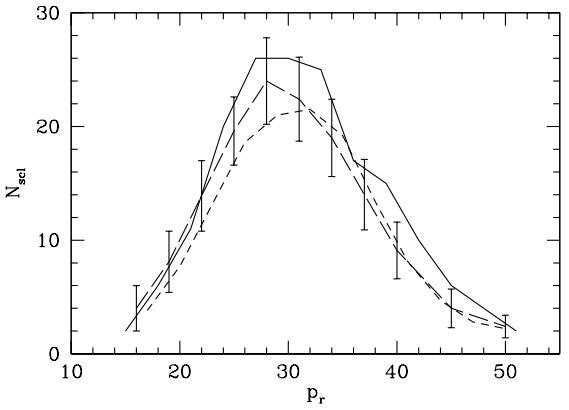

Figure 1. Number of superclusters $N_{\rm scl}$ as a function of $p_{\rm r}$ for both data and the two DM models. Solid line denotes the observational sample, while dashed and dotted lines correspond to the two models (ΛCDM, τCDM). Note that the superconnectivity limit is similar in all three datasets, occurring at depths $> 33h^{-1}$ Mpc. Errorbars ($\pm 1\sigma$) are shown only for one set of data for clarity.

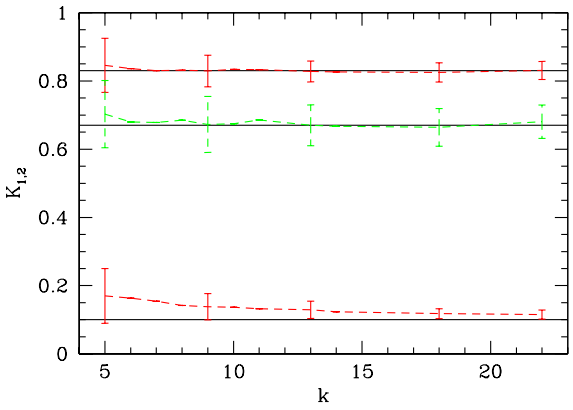

Figure 2. Performance of shapefinders K_1, K_2 as a function of multiplicity k. Theoretical values (horizontal solid lines) are compared with MC computed ones (dashed lines with errorbars) for two ideal objects, i.e. a pancake (upper and lower lines denoting K_1 and K_2 respectively) and a triaxial object (middle line showing K_1). Errors correspond to the $\pm 1\sigma$ scatter from 100 MC realizations performed for each k, shapefinder and object separately.

ter samples as a function of radial depth. This is of prime significance since construction of mock cluster catalogues will be based on the above parameter. We do so by using ten equal volume shells ($\delta V \approx 3 \times 10^6\, h^{-3}$ Mpc^3) up to $R_{\rm max} \leq 315h^{-1}$ Mpc and calculate the individual densities of the two observational catalogues separately. The corresponding average-over-shells densities for the two samples are $n_{\rm Abell} \sim 1.62 \times 10^{-5} h^3\,{\rm Mpc}^{-3}$ and $n_{\rm ACO} \sim 2.55 \times 10^{-5} h^3\,{\rm Mpc}^{-3}$, giving rise to intercluster separations of order $\sim 39.5h^{-1}$ Mpc and $\sim 34h^{-1}$ Mpc respectively. For completeness, we note that the number density of the combined catalogue is $\sim 1.82 \times 10^{-5} h^3\,{\rm Mpc}^{-3}$ corresponding to a mean separation of $\sim 38h^{-1}$ Mpc in accordance with other estimates of the same population.

3.2 The shapefinders

An appreciable number of geometrical and topological tools have been developed recently for identifying correctly and quantifying the rich texture of large scale structure as it appears in large angular or redshift surveys and N-body simulations (Babul & Starkman 1992; Luo & Vishniac 1995; Sahni & Coles 1995; Sahni 1998; Sathyaprakash et al. 1998b and references therein). In contrast to traditional schemes (low-order statistics) which bear no relation to either topology nor shape, the shapefinders have been constructed from Minkowski functionals (volume V, surface area S, integrated mean curvature C and genus G) in an attempt to discriminate between complex morphologies such as filaments (prolate-like objects), pancakes (oblate-like objects), triaxial structures (ribbons) and spheres (see Figure 1 of Sahni et al. 1998 and Figure 2 of Sahni 1998 for a schematic presentation of the above morphological categories).

For a particular surface of integration class $\mathcal{C}^2$ it is well known that we can define the four Minkowski functionals which completely characterise the geometry as well as the topology of a compact surface. We, thus, introduce the three shapefinders $\mathcal{H}_1 = VS^{-1}$, $\mathcal{H}_2 = SC^{-1}$ and $\mathcal{H}_3 = C$ having dimensions of length. Based on these, we can further define the two dimensionless shapefinders K_1 and K_2 as follows:

$$K_1 = \frac{\mathcal{H}_2 - \mathcal{H}_1}{\mathcal{H}_2 + \mathcal{H}_1} \qquad (1)$$

and

$$K_2 = \frac{\mathcal{H}_3 - \mathcal{H}_2}{\mathcal{H}_3 + \mathcal{H}_2}\ , \qquad (2)$$

where $K_{1,2} \leq 1$ by definition.

Therefore, having identified superclusters using the specified percolation radius, shape detection is performed only for those objects having $k \geq 8$ members via the moments of inertia method. By fitting the best triaxial ellipsoid with parametric form

$$\boldsymbol{r}(\theta,\phi) = I_1 \sin\theta\cos\phi\,\hat{\boldsymbol{i}} + I_2 \sin\theta\sin\phi\,\hat{\boldsymbol{j}} + I_3\cos\theta\,\hat{\boldsymbol{k}}\ , \qquad (3)$$

to real and mock data, we can obtain the three eigenvalues I_1, I_2, I_3, which directly relate to the three principle axes of the fitted ellipsoid. The volume can be then defined as $V = \frac{4\pi}{3} I_1 I_2 I_3$ and $0 \leq \phi \leq 2\pi$, $0 \leq \theta \leq \pi$. Subsequently, the latter parameters can further be used to derive the shapefinders $\mathcal{H}_{\rm i}$ and $K_{\rm i}$.

The above shape technique characterises the shapes of topologically non-trivial cosmic objects according to the following classification:

(i) Pancakes if $K_1/K_2 > 1$
(ii) Filaments if $K_1/K_2 < 1$
(iii) Triaxial structures if $K_1/K_2 \approx 1$ and
(iv) Spheres if $I_1 = I_2 = I_3$ and $K_1 \approx K_2 \approx 0$.

Ideal filaments (0,1), pancakes (1,0), triaxial structures (1,1) and spheres (0,0) are represented by the four vertices of the shape plane in the form of the shape vector $K = (K_1, K_2)$, whose amplitude and direction determines the morphology of an arbitrary 3D surface. Fi-

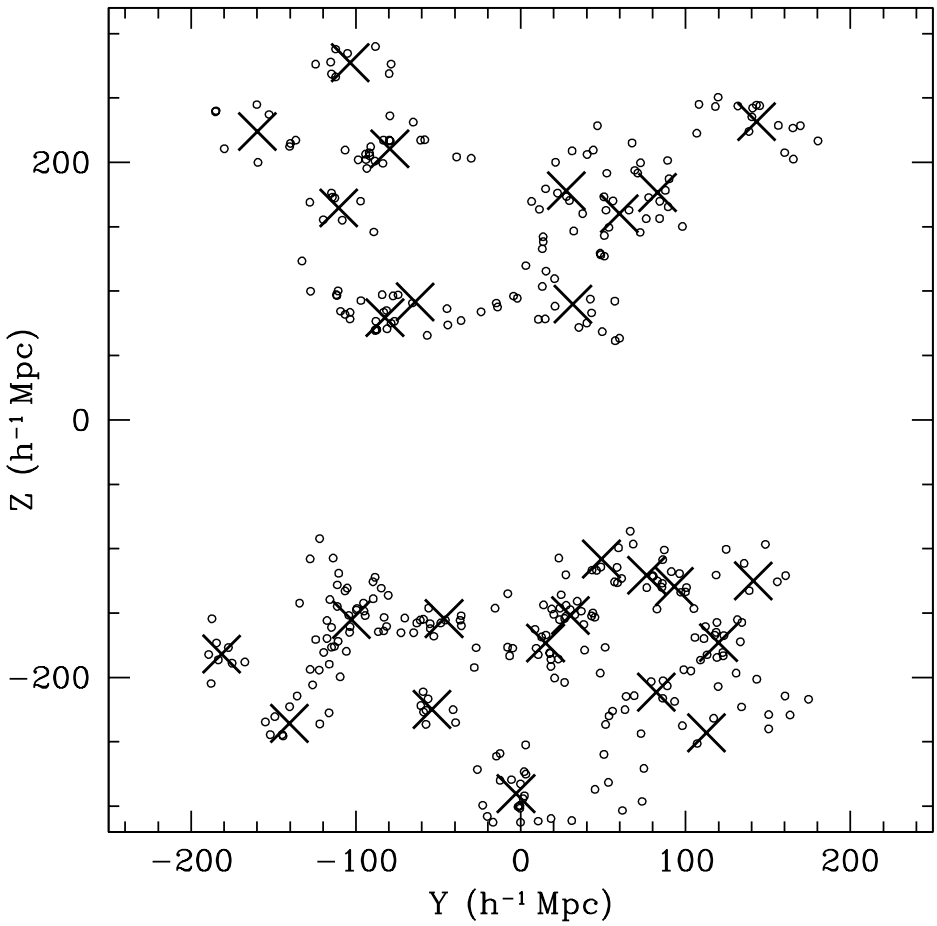

Figure 3. Two dimensional whole sky map of the 26 Abell/ACO superclusters (crosses). Open symbols denote the clusters associated with superclusters with $k \geq 8$. Note, that we have detected 11 superclusters in the North and 15 in the South.

nally, for shapes close to spherical, K_1 and K_2 are very small, so that it is meaningful to measure their ratio $\mathcal{R} = K_1/K_2$ and evaluate deviations from sphericity (for further details see section 4.2 of BPR).

3.3 Stability of the method

The present study is based on superclusters with $k \geq 8$, as quoted above. This choice has been made on stability grounds and is a compromise between adequate statistics and efficiency of the shape technique (see Plionis, Barrow & Frenk 1991; Jaaniste et al. 1998 their section 3.2). Indeed, it has been established that superclusters shape properties are accurately estimated as long as $k \geq 8$ members (Jaaniste et al. 1998 their figure 2). In order to investigate the performance of our shape finding method, we utilise a Monte Carlo (MC) approach. In particular, given as input parameters the three axes I_1, I_2 and I_3 of an ellipsoid with equation

$$\frac{x_1^2}{I_1^2} + \frac{x_2^2}{I_2^2} + \frac{x_3^2}{I_3^2} \leq 1 \qquad (4)$$

for $k \geq 5$, the question that we answer is "what are the most probable measured K_1, K_2 recovered by our shape algorithm?"

In Figure 2, we compare theoretical predictions with MC estimated values of K_1 and K_2 as a function of multiplicity k. Horizontal solid lines correspond to the input values for an ideal pancake (upper and lower) and an ideal triaxial structure (middle) and are taken from Sahni et al. (1998 their Table 1). Upper (K_1) and lower (K_2) dashed lines with errorbars denote the derived figures for the pancake, while the middle one (K_1) indicates the triaxial object. For the latter case, we observe that our MC computed values always approximate extremely well (within 5%) the input ones for all multiplicities used. Similar results are also obtained for K_1 in the case of the pancake (upper lines). Nevertheless, it is evident that our K_2 estimated figures lie systematically above the input ones, albeit asymptotic convergence is gradually restored. This systematic trend effectively means that our algorithm tends to make pancakes less planar, a feature which is more pronounced at small multiplicities. Exactly the opposite event occurs in the case of filaments for the input and MC estimated values of K_1, thus producing less elongated filaments than it

should. This effect tends to produce a slightly distorted shape spectrum of superclusters, keeping, however, the shape identity of the sample unchanged (filaments remain filaments and pancakes remain pancakes).

We have concluded that, for $k < 8$, our input results differ significantly from the MC computed values for the study cases of the pancake (K_2) and the filament (K_1). This is also in line with previous analyses on shape determination, thus proving the caveat of the technique for superclusters with a few cluster members.

4 MORPHOLOGICAL PROPERTIES

4.1 The Abell/ACO supercluster features

We investigate supercluster characteristics according to the observational requirements and the definitions of shape diagnostics set in section 3. Taking the optimum value of $p_{\rm r} = 27h^{-1}$ Mpc for the combined Abell/ACO sample, we end up with 26 superclusters with $k \geq 8$. The relevant information is presented in Table 2. In Figure 3, we show a 2D schematic representation of superclusters (crosses) superimposed onto the related cluster distribution (open symbols) for the observed sample. The absence of objects in the central stripes of the plot is due to the ZoA restrictions that we have placed. Note, that only objects with $k \geq 8$ are plotted.

As is evident from Table 2, there are no spherical superclusters in concordance with numerical N-body simulations of gravitational clustering and similar studies on observed data (Plionis et al. 1992; Sathyaprakash et al. 1998a, b; Sahni et al. 1998; BPR). More than half of the systems (54% or 14/26) reveal filamentary structure (cf. section 5.2), 5 of which are dubbed as extreme filaments ($\mathcal{R} \leq 0.5$). The rest of the objects (12 or 46%) are estimated to be pancakes, with 2 of them being extreme cases ($\mathcal{R} \geq 2$).

We plot in Figure 4 the results of this study, where the ratio $\mathcal{R}$ as a function of k is shown for all 26 real superclusters. The equilibrium between filamentarity and planarity, however, seems to be perturbed if we extend the k infimum from 8 to 10 members. In this case, we find 71% (12/17) filaments, while for $k \leq 10$ superclusters we obtain 64% (7/11) pancakes. We attribute this to the ill-defined shapes, as evidenced from the analysis of section 3.3 (cf. Figure 2). We thus observe that low k superclusters are mostly compatible with pancakes or extreme pancakes (see object at the upper left of Figure 4), whilst large ones are better described as filaments or extreme filaments. Statistically speaking, the larger the multiplicity, the more accurately supercluster morphologies are defined, the more filaments are revealed.

4.2 The simulated distributions

The task of constructing mock supercluster catalogues based on the two aforementioned DM models (τCDM, ΛCDM) is accomplished by using the selection parameters of the Abell/ACO population presented earlier. Since the lengths of the simulated boxes are $2h^{-1}$ Gpc and $3h^{-1}$ Gpc for the two models respectively, we can

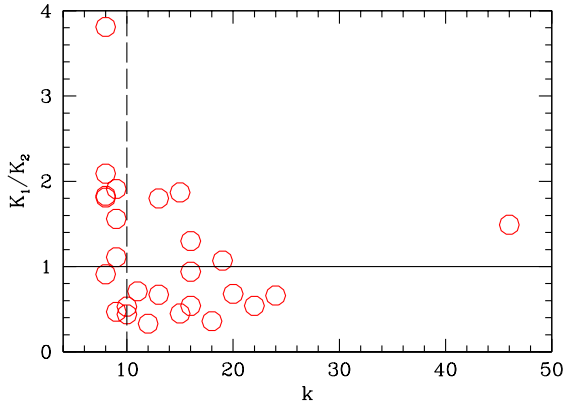

Figure 4. Ratio $\mathcal{R}$ as a function of multiplicity k for the 26 real superclusters. The vertical dashed line corresponds to the k-cut discussed in text and the horizontal one splits the regions of filaments and pancakes.

easily define several mock cluster distributions as seen by a variety of totally independent observers. The number of these observers per simulation box can then be computed as $N_{\rm obs} = (L_{\rm box}/2R_{\rm max})^3$. For τCDM, we have defined 27 such observers and 64 for ΛCDM, each of them having exactly the same observational features as the initial Abell/ACO population (i.e. number density, number of clusters, selection function, geometry and $R_{\rm max}$).

We, furthermore, make use of the percolation parameter $p_{\rm r}$ that maximises the mock supercluster numbers for each model (see Figure 1). For τCDM, we have computed $p_{\rm r} = 32h^{-1}$ Mpc and $p_{\rm r} = 28h^{-1}$ Mpc for ΛCDM. The latter figures correspond to $\sim 21.5 \pm 3.5$ superclusters for τCDM and $\sim 24 \pm 4$ for ΛCDM, where means and scatters emanate from the 27 and 64 observers respectively.

It is evident that the choice of $p_{\rm r}$ both for the models and the observational data is essential not only for the detection of rich superclusters, but for getting a better handle on cosmic variance effects as well (see next section). To this end, we have cross checked our findings using the nearest neighbour statistical measure (critical radius $R_{\rm cr}$) for clustered distributions (Peebles 2001)

$$R_{\rm cr} \simeq \left[\frac{3-\gamma}{\omega_{\rm s}\langle n\rangle r_\circ^\gamma}\right]^{\frac{1}{3-\gamma}} , \qquad (5)$$

where $\omega_{\rm s}$ and $\langle n\rangle$ are the solid angle and mean number density and $r_\circ$, γ correspond to the correlation length and the slope of the correlation function of the sample under study. Using a plausible set of parameters for the clustering properties (correlation lengths, amplitudes and slopes) of the two models (see section 3.2 of Colberg et al. 2000) and the average values from the literature for the observed sample, we find that our figures are very well computed and in excellent agreement with those predicted by equation (5).

5 SUPERCLUSTER STATISTICS

Table 2. List of the Abell/ACO superclusters using $p_r = 27h^{-1}$ Mpc. The correspondence of the columns is as follows: index number, multiplicity, axes of triaxial ellipsoid, distance from us, K_1, K_2, their ratio $\mathcal{R}$, the morphological classification type and finally the supercluster name (see Einasto et al. 2001a their Table A1). F denotes filaments, P is for pancakes and eF and eP symbolise extremely elongated or planar superclusters. Note that I_1, I_2, I_3 and R have units of h^{-1} Mpc. We also report that due to our cut in b, only part of the Shapley supercluster has been detected.

Index	k	I_1	I_2	I_3	R	K_1	K_2	$\mathcal{R}$	Type	Name
1	16	91.6	26.8	14.1	267.9	0.1405	0.2622	0.54	F	Pegasus-Pisces + Aquarius
2	22	63.0	30.6	25.1	291.0	0.0416	0.0773	0.54	F	Sculptor
3	11	37.1	20.5	14.8	184.1	0.0454	0.0644	0.71	F	Pisces - Aries
4	9	31.1	23.1	12.1	129.1	0.0723	0.0463	1.56	P	Pisces
5	24	56.7	23.8	14.1	174.1	0.0945	0.1429	0.66	F	Pisces - Cetus
6	8	30.8	20.4	3.1	302.4	0.4551	0.1194	3.81	eP	Fornax - Eridanus
7	18	84.9	19.0	11.7	117.8	0.1206	0.3355	0.36	eF	Sextans + Leo
8	8	34.5	21.2	7.7	204.3	0.1778	0.0972	1.83	P	Leo - Sextans
9	13	55.9	22.3	12.6	185.6	0.1074	0.1614	0.67	F	Ursa Majoris
10	9	44.8	22.5	10.3	298.0	0.1356	0.1218	1.11	P	Leo - Virgo
11	19	63.1	34.6	17.9	225.5	0.1004	0.0938	1.07	P	Virgo - Coma
12	9	36.1	22.1	7.7	275.3	0.1913	0.1001	1.91	P	Leo A
13	16	42.0	27.1	18.2	295.5	0.0431	0.0458	0.94	F	Draco
14	15	47.7	33.0	13.5	135.1	0.1333	0.0712	1.87	P	Shapley (part)
15	16	55.7	37.1	20.2	184.8	0.0742	0.0570	1.30	P	Bootes
16	10	35.0	14.3	9.9	210.6	0.0713	0.1336	0.53	F	Corona Borealis
17	15	56.5	19.3	13.2	116.2	0.0835	0.1843	0.45	eF	Hercules
18	10	37.6	13.7	10.3	240.6	0.0680	0.1545	0.44	eF	Aquarius B
19	9	27.1	11.5	9.6	168.0	0.0488	0.1048	0.47	eF	Aquarius-Cetus
20	20	71.9	38.7	28.3	233.8	0.0460	0.0681	0.68	F	Aquarius
21	8	33.1	18.3	5.1	190.5	0.2757	0.1317	2.09	eP	-
22	46	79.6	59.3	32.4	189.7	0.0638	0.0428	1.49	P	Horologium - Reticulum
23	8	33.9	19.4	6.6	285.2	0.2069	0.1141	1.81	P	Caelum
24	12	43.5	10.9	8.0	263.3	0.0892	0.2733	0.33	eF	Microscopium
25	13	45.2	30.7	12.8	205.9	0.1306	0.0726	1.80	P	-
26	8	31.3	17.3	10.3	277.8	0.0737	0.0806	0.91	F	Grus

5.1 Cosmological implications

We compare the shape and volume (size) spectrum distributions between the data and two cosmological models via a standard Kolmogorov-Smirnov (KS) statistical test. We then compute the corresponding probabilities of consistency between models and data ($\mathcal{P}_{\rm KS}$) and place these results in Table 3. In order to investigate whether the above two statistics can be used as a cosmological discriminant, we firstly use the KS test so as to compare the two model distributions. It is evident from Table 3 that the shape spectrum fails to discriminate between the two models, probably echoing the Gaussian initial conditions common to both cosmologies. The volume spectrum constitutes a useful tool, since it yields a zero probability ($\sim 10^{-19}$) that τCDM and ΛCDM are being selected from the same parent population.

We display in Figure 5 the results from the shape (left plots) and volume (right plots) spectrum. Upper panels correspond to the τCDM model and lower to ΛCDM. Hatched areas and open symbols denote the observed data and filled circles are for the two DM cosmologies. Errorbars in all panels are the $\pm 1\sigma$ values based on the independent observers and the vertical solid lines in the left mark the transition limits between filaments and pancakes. A characteristic worth observing is that in both models the percentage of filaments exceeds that of pancakes. The latter finding is in accordance with N-body results (Sathyaprakash et al. 1998a, b). A clear indication of the discriminative power of the volume spectrum test is presented in the right panels of Figure 5. It is apparent that the τCDM distribution gives the worst fit to the observed data with probability of consistency being a mere 0.001. In contrast to this, it seems that the volume spectrum of ΛCDM superclusters better represents that of the Abell/ACO supercluster sample with corresponding probability of consistency being 0.271. This can be explained by regarding the volume spectrum as a natural outcome of the different clustering pattern of the two cosmologies considered here (see Jenkins et al. 1998; Colberg et al. 2000 for a comparison between optical data and Virgo models).

Table 3. KS probabilities ($\mathcal{P}_{\rm KS}$) of consistency between data and models as well as between the two DM models. Note, that in this computation, we have used the total number of mock superclusters identified within all independent volumes for the two models.

Pair	Sh. Spectrum	Vol. Spectrum
Real - ΛCDM	0.682	0.271
Real - τCDM	0.488	0.001
ΛCDM - τCDM	0.242	$\sim 10^{-19}$

To validate our findings, we further explore the selection parameters presented in section 3 and test the

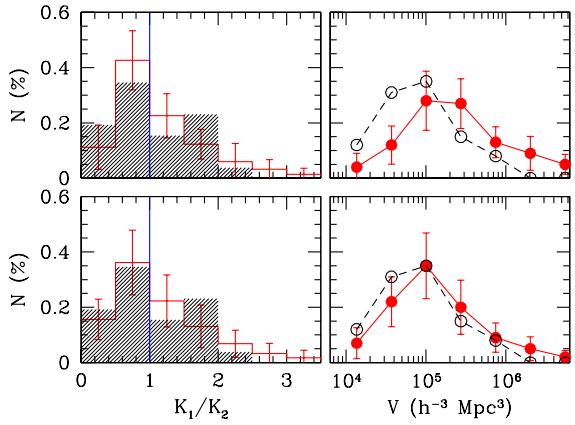

Figure 5. Statistical comparison between data (hatched areas and open circles) and models (filled symbols). Shape spectra are plotted in left panels and multiplicity functions in right for τCDM (top) and ΛCDM (bottom) respectively.

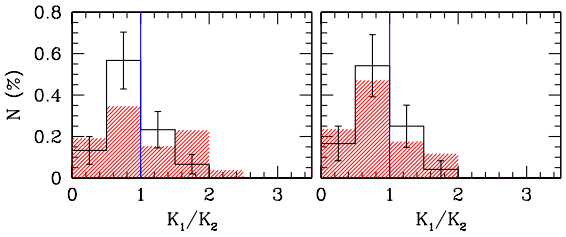

Figure 6. Shape distributions for Abell/ACO (hatched areas) and PSCz superclusters for $k \geq 8$ (left) and $k \geq 10$ (right). Poissonian errors are only shown for the PSCz sample for clarity.

reliability of our methods. On choosing reasonable values for $p_{\rm r}$, the multiplicity infimum and finally a smaller set of independent observers, we have recovered that results remain remarkably robust.

5.2 Optical vs Infrared supercluster shapes

We attempt to compare the shape spectrum of the optical (Abell/ACO) and the infrared (PSCz) superclusters in order to probe whether or not the prominence of filamentarity is retained by all-sky data with diverse global geometrical and selection properties. For this purpose, we have resorted to the recently constructed all-sky PSCz supercluster catalogue (BPR) counting ~ 12000 infrared galaxies.

We display in Figure 6 the shape distribution of infrared and optical data (hatched histograms) for superclusters with $k \geq 8$ (left) and $k \geq 10$ (right). It is obvious that the filamentarity dominance is confirmed by both kinds of data, although it is less prominent in our optical sample for $k \geq 8$ (cf. Figure 4 and discussion in section 4.1). In fact, for $k \geq 10$, we observe that infrared and optical data yield almost identical values for the fractions of filaments ($\sim 70\%$) and pancakes ($\sim 30\%$).

A final word of caution is due here. The above argument is not to cast any shadow on the results based on the use of the nominal k infimum applied to the present analysis. Had we used superclusters with $k \geq 10$, we would have obtained qualitatively the same results but run the risk of being too close to the validity limit of the KS test.

6 CONCLUDING REMARKS

We have explored the shape parameters of superclusters identified in observed optical (Abell/ACO) and simulated (Virgo DM models) cluster populations, up to a depth of $315h^{-1}$ Mpc. We have applied a constant size percolation radius $p_{\rm r}$ to both data and DM models in order to detect superclusters within the volumes of the given cluster samples. Using the selection features of the Abell/ACO catalogue, we have constructed several mock supercluster samples based on independent observers for the two cosmological models (τCDM and ΛCDM). The investigation of supercluster morphologies has been based on a differential geometry method devised by Sahni et al. (1998a).

Results indicate that filamentary structures dominate the volumes considered here over pancake morphologies, as seen in both data and models. This, further supports the idea that filamentarity is the main structural feature of large scale structure, since it has been reliably detected in all available infrared and optical samples analysed up to date. No spherical superclusters are detected in accordance with similar observational analyses and theoretical predictions from large N-body experiments (Sathyaprakash et al. 1998a; BPR).

A standard KS statistical test of consistency between data and the two models on the size distributions has clearly given a preference to the ΛCDM ($\Omega_\Lambda = 0.7$) cosmology. On the contrary, τCDM is rejected at a high (99.9%) significance level. Finally, the shape spectrum is insensitive to the two cosmologies, reflecting their common Gaussian initial conditions. The latter findings are in concordance with a similar analysis based on infrared PSCz supercluster properties.

ACKNOWLEDGEMENTS

We have made use of two cosmological models extracted from the Virgo Consortium simulations following the public release of the available data (Frenk et al. 2000). The Hubble Volume cluster catalogues can be found in http://www.mpa-garching.mpg.de/Virgo/.

REFERENCES

Abell G., 1958, ApJS, 3, 211
Abell G., Corwin H., Olowin R., 1989, ApJS, 70, 1
Babul A., Starkman G., 1992, ApJ, 401, 28
Bahcall N., Soneira R., 1984, ApJ, 277, 27
Bahcall N., Ann. Rev. Astr. Ap., 26, 631
Basilakos S., Plionis M., Rowan-Robinson M., 2001, MNRAS, 223, 47 (BPR)
Batutski D., Burns J., 1985, AJ, 90, 1413
Cappi A., Maurogordato S., 1992, A&A, 259, 423

Colberg J. et al., 2000, MNRAS, 319, 209
Davé R., Hellinger D., Primack J., Nolthenius R., Klypin A., 1997, MNRAS, 284, 607
de Lapparent V., Geller M. J., Huchra J. P., 1991, ApJ, 369, 273
Einasto M., Einasto J., Tago E., Dalton G., Andernach H., 1994, MNRAS, 269, 301
Einasto M., Tago E., Einasto J., Andernach H., 1997, A&AS, 123, 119
Einasto M., Einasto J., Tago E., Mueller V., Andernach H., 2001a, astro-ph/0012536
Einasto M., Einasto J., Tago E., Andernach H., Dalton G., Mueller V., 2001b, astro-ph/0012538
Eke V., Cole S., Frenk C. S., 1996, MNRAS, 282, 263
Evrard A. et al. 2001, ApJ, *submitted*, astro-ph/0110246
Frenk C. et al., 2000, MNRAS, astro-ph/0007362
Frisch P. et al., 1995, A&A, 296, 611
Jaaniste J., Tago E., Einasto M., Einasto J., Andernach H., Mueller V., 1998, A&A, 336, 35
Jenkins A. et al., 1998, ApJ, 449, 20
Kalinkov M., Kuneva I., 1995, A&AS, 113, 451
Kerscher M. et al., 1997, MNRAS, 284, 73
Kerscher M., Mecke K., Schmalzing J., Beisbart C., Buchert T., Wagner H., 2001a, A&A, 373, 1
Kerscher M. et al., 2001b, A&A, 377, 1
Luo S., Vishniac E., 1995, ApJS, 96, 429
Mecke K., Buchert T., Wagner H., 1994, A&A, 288, 697
Peebles P. J. E., 2001, ApJ, 557, 495
Plionis M., Valdarnini R., 1991, MNRAS, 249, 46
Plionis M., Barrow J.D., Frenk C.S., 1991, MNRAS, 249, 662
Plionis M., Valdarnini R., Jing Y. P., 1992, ApJ, 398, 12
Postman M., Huchra J., Geller M., 1992, ApJ, 384, 404
Sahni V., 1998, in Sato K., editor, Proceedings of the IAU symposium No. 183, Kyoto, Japan, astro-ph/9803189
Sahni V. & Coles P., 1995, Phys. Rep., 262, 1
Sahni V., Sathyaprakash B. S., Shandarin S., 1998a, ApJ, 495, L5
Sathyaprakash S. B., Sahni V., Shandarin S., 1998b, ApJ, 508, 551
Sathyaprakash S. B., Sahni V., Shandarin S., Fisher B. K., 1998a, ApJ, 507, L109
West J. M., 1989, ApJ, 347, 610
Yess C. & Shandarin S., 1996, ApJ, 465, 2
Zeldovich, Ya. B., Einasto, J., Shandarin, S., 1982, Nature, 300, 407
Zucca E., Zamorani G., Scaramella R., Vettolani G., 1993, ApJ, 407, 470